Multi-Element Strain Gauge Modules for Soft Sensory Skins

Edward L. White, *Student Member, IEEE*, Jennifer C. Case, *Student Member, IEEE*, and Rebecca K. Kramer, *Member, IEEE*

***Abstract*— In this paper, we describe the fabrication and testing of a sensory module composed of resistive strain gauges in an elastomer substrate. Each module contains three resistive gauges, providing sufficient information to reconstruct the geometry of the module. The modules are fabricated from two bonded sheets of silicone elastomer. The sensing element is a resistive strain gauge based on room-temperature liquid gallium–indium alloy contained within microchannels in the substrate. We demonstrate the functionality of the module by mechanically stretching it over a template and measuring the change in resistance of the embedded liquid metal strain gauges. Starting with known strains, we calibrate the device and fit a quadratic model. With the model and the measured error distribution, we can predict the uncertainty in the reconstructed position of the corners of the triangular modules, which we refer to as nodes.**

***Index Terms*— Mechanical sensors, wearable sensors, sensor arrays, displacement measurement, electrical resistance measurement.**

I. Introduction

THE field of soft robotics presents the opportunity to create devices with capabilities totally unlike those achieved by traditional robotic systems. As soft robots are built from highly deformable materials, the joint-linkage paradigm found in rigid robots breaks down. The result is robotic systems with infinite degrees of freedom. The downside of flexibility comes in the area of control. Instead of observing and controlling a fixed number of states, soft robots have a much more challenging problem, namely the need to observe a deformation across the entire soft body. In order to provide this proprioceptive feedback, distributed sensors are required. These sensors can either be embedded in the body of a robot, or placed on the exterior as a skin. The latter approach is what we pursue in this work.

In this paper, we describe the fabrication and testing of sensory skin modules shown in Fig. 1. Each module is composed of an array of resistive strain gauges placed along the edge of its body, providing complete definition of its current state. These modules could be applied to the exterior of a soft robot to measure the state of deformation at that location in the robot body. Furthermore, this module design could be applied to other deformable planar systems, such as wearables, or used to measure state in traditional robots. To measure state over a larger soft robot body, arrays of these modules could be connected together, creating large-area sensory skins. The size of the sensory skin modules described makes them applicable to larger systems, for example human-scale robots and wearable devices. We selected a triangular geometry since multiple triangular elements can be used to "mesh" a surface without ambiguity in the resulting configuration. Geometries with more edges require more strain measurements than the number of nodes to define the geometry. For example, a square requires five measurements to define the location of four nodes. This concept is illustrated in Fig. 2.

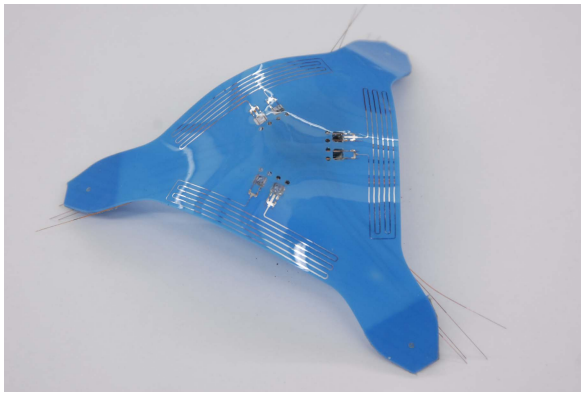

Fig. 1. A completed module, showing resistive strain gauges made from conductive liquid metal encapsulated in microchannels. The microchannels are embedded between two elastomers: SIL-950, which is opaque (blue), and Sylgard 184, which is transparent, rendering the liquid metal visible between layers.

We have two goals with this paper. First, we aim to demonstrate an approach to manufacturing modules which can be scaled to produce large numbers of devices. Second, we aim to demonstrate state reconstruction through resistive strain measurements. To support the first goal, the modules were fabricated with a laser-based moldless patterning process that is much more scalable than traditional soft microchannel patterning approaches. Microchannels were patterned directly into cured elastomer substrates, rather than curing elastomer in molds. These microchannels were filled with liquid gallium indium alloy, forming the resistive sensing element of the strain gauges. To support the second goal, we calibrated the

Manuscript received October 20, 2015; accepted November 24, 2015. Date of publication December 10, 2015; date of current version February 24, 2016. This work was supported by the National Aeronautics and Space Administration within the Early Career Faculty Program through the Space Technology Research Grants Program under Grant NNX14AO52G. The work of E. L. White was supported by the National Science Foundation Graduate Research Fellowship under Grant DGE-1333468. The associate editor coordinating the review of this paper and approving it for publication was Prof. Ravinder S. Dahiya.

The authors are with the School of Mechanical Engineering, Purdue University, West Lafayette, IN 47907 USA (e-mail: white335@purdue.edu; case15@purdue.edu; rebeccakramer@purdue.edu).

Digital Object Identifier 10.1109/JSEN.2015.2507540

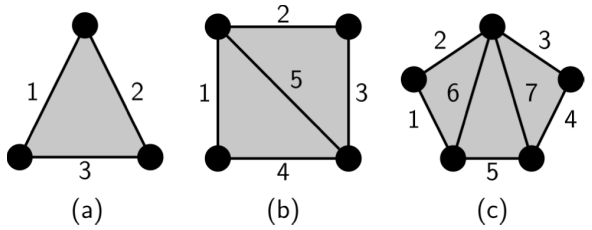

Fig. 2. Schematic illustration of a (a) 3-sided element, (b) 4-sided element, and (c) 5-sided element. Each solid line represents a length which must be measured for the geometry of the nodes to be uniquely defined in two dimentional space. The numbers correspond to these solid lines. The triangle requires three measurements, the square requires five measurements, and the pentagon requires seven measurements. Thus, the triangular element has an equal number of measurements and nodes, the square requires one more measurement than nodes, and the pentagon requires two more measurements than nodes.

modules against known positions, then recovered the geometry for unknown positions using measurements of resistance.

The strain sensing elements in our design are placed at the edge of the structure to maximize their sensitivity to deformation and to reduce cross-talk between channels as much as possible. Ideally, we would have created a single channel directly between two nodes. This was not possible for two reasons. First, we wish to increase the overall length of the microchannels to increase their resistance, making them easier to interface with and measure. Second, we wish to offset the sensors from the node-to-node line so that multiple triangular elements could be attached together without mechanical interference. Beyond these considerations, the design of the sensor array and the microchannels was dictated by our manufacturing capabilities, which include the minimum trace width, the minimum spacing between traces, and the minimum distance from the edge of the module to a microchannel. The minimum channel width is determined by two effects: the capability of the laser used in this study to fabricate the channels, and the minimum size channel through which eutectic gallium indium will spontaneously reflow. The minimum spacing between channels is dictated by bonding between elastomer layers. As the elastomer substrates are patterned, a small region of the substrate near the microchannel becomes ablated by the laser patterning process and does not support good adhesion between layers. Microchannels must be kept far enough apart so that there is un-ablated elastomer between the channels. The minimum spacing between a channel and the edge of the module is based on the alignment accuracy achieved by manually aligning modules in the laser patterning system. Doubling or halving these limits would not result in a significant impact to the overall design of the module.

II. Previous Work

The field of sensory skins is populated with many different approaches and design goals. Some of these devices are intended to sense the external environment, some are intended to capture some form of user input or other robot-environment interaction, and some are designed to provide feedback on the current state of the system. Our design falls into this last category; it is intended to provide proprioceptive feedback in a soft robotic system. The field of polymer MEMS, which includes sensory skin applications, was reviewed by Liu [1]. Biological sensing applications, including artificial skin, were reviewed by Nambiar and Yeow [2]. More specifically, stretch sensors for human applications were reviewed by O'Brien, *et al.* [3]. Our review of sensory skins parallels the development of the field. We first discuss flexible polymer substrates used to hold together separate sensing elements. Next, we describe how flexible polymer itself was transformed into a sensing element. We continue on to discuss the emergence of conductive polymer composites, which are an alternative approach to creating soft sensory skins. Finally, we review stretchable sensory skins and discuss how conductive elements may be integrated into soft substrates.

One of the first polymeric materials used in sensory skins was polyimide, which has proven to be a versatile material, serving as both an inert substrate supporting active elements and as a part of the sensing elements themselves. As a supporting element, polyimide has been used to support hotwire anemometers [4], silicon force sensors [5], and shear sensors for aerospace and underwater applications [6], [7]. As a sensing element, membranes of polyimide have been used in resistive force gauges [8], [9], multi-mode sensory skins, with temperature, thermal conductivity, force, and stiffness sensors [10], and multi-axis force sensors [11]. Thicker polyimide structures have recently been demonstrated with improved reliability over their thin membrane counterparts [12], [13]. One of the challenges associated with using polyimide film as a substrate is its limited stretchability. One approach to increasing the maximum strain of the material is through a lattice-like structure of polyimide and metal film [14]. We have opted to use a stretchable elastomer instead of a flexible polymer since the former is more mechanically compatible with soft systems, including elastomer robots and biological systems such as humans.

The examples presented above all used metal films as resistive sensing elements. An alternative is to create conductive polymer composites, which have the advantage of supporting larger strains than metal. Conductive composites have been fabricated in arrays of dots on a polyimide substrate to sense force over a surface [15]. A hybrid approach can also be used, combining a single conductive polymer composite with metal addressing electrodes [16], [17]. In addition to measuring changes in resistance, alternative sensing mechanisms have been described. Variable gain in a field effect transistor [18] and changes in capacitance have also been used to measure applied loads in polyimide systems [19]. In this work, we have opted to use resistance-based measurements of strain due to the simple electrical interface required. Further, we have elected not to use conductive composites due to their lower conductivity and reduced mechanical and electrical stability over multiple cycles [20].

Although polyimide is flexible, it is not stretchable, making it of limited use in our current application, where high planar deformation is required. Polyimide has been frequently employed as a base for MEMS-inspired sensor skins due to its material compatibility with MEMS processing. For example, it can be polymerized in place, making it attractive for spin coating thin features such as membranes

and connective layers. It is also more likely to already be found in semiconductor processing equipment, such as metal evaporators. Despite these advantages, we see the mechanical limitations of polyimide as outweighing the benefits from simpler processing. We believe that this present work describes an approach to using elastomers that is highly scalable and overcomes some of the fabrication challenges that may have restricted adoption of elastomers in the past.

As an alternative to inextensible polymers, stretchable elastomers can be used to fabricate the entire sensory skin. One of the most popular is silicone rubber. The most common of these rubbers is Sylgard 184 from Dow Corning, which is a polydimethylsiloxane (PDMS). Other popular silicones are EcoFlex and DragonSkin, both from Smooth-On. Unlike in polyimide sensors, metal films are mechanically incompatible with the high deformations present in these soft polymers. Instead, the polymer itself can be turned into a sensing element by forming a conductive polymer composite by adding carbon black [21] or expanded intercalated graphite to the bulk material [20], or by depositing carbon nanotubes [22]–[24], silver nanowires [25], or graphene-nanocellulose on the surface of the elastomer [26]. In summary, there are many different combinations of conductive and silicone materials which can be combined together. There are trade-offs that drive material selection and the choice of loading. These include the changes in material properties that occur due to the inclusion of the harder and stiffer conductive phase, the decrease in strength that occurs due to stress concentration, the bulk conductivity of the material, and the gauge factor. As we noted previously, we have elected not to use conductive composites in this application due to the degradation of mechanical and electrical properties over the base elastomer.

An alternative approach to using a solid conductor is to use a liquid. Within the soft robotics community, the room-temperature liquid metal alloy of gallium and indium is a popular choice due to its mechanical compatibility with elastomeric structures [27]. Liquid-metal-filled microchannels have been used to measure biaxial stretch and applied pressure [28]–[31], curvature [32], and joint angle [33], and have been integrated with shape memory alloy to create an active skin [34]. Liquid-metal-based sensors are fundamentally different from most of the polyimide sensors described earlier since they are able to measure the state of the sensor body, and not only the applied loads. This is functionally similar to what we are demonstrating in this current work, since our focus is on proprioceptive sensing.

In these devices, as in the work presented here, hollow microchannels were created in a silicone substrate, then filled with liquid metal. However, we are also working to develop more scalable approaches. Our group has previously demonstrated fabrication of strain sensors by direct writing liquid gallium indium alloy followed by encapsulation in PDMS [35]. We have also demonstrated ink jetting of an ethanol-based ink containing sub-micron scale particles of liquid metal [36]. These two processes, along with the laser-based approach described in this work, are all attempts to increase the manufacturablity and reliability of liquid-metal. As these alternative approaches to patterning liquid metals mature, we intend to create devices such as those we describe in this work with the new methods.

Resistive liquid metal sensors are not the only approach to creating soft sensor skins. Alternatives resistive approaches include the use of conductive solutions [37] and ionic liquids [38]. With proper integration, metals can be used in silicone substrates, with similar geometries to those discussed previously in polyimide, resulting in capacitive force sensors [39], dual-mode force and proximity sensors [40], and multi-mode strain, touch and pressure sensors [41]. Hybrids of soft elastomers and flexible polymers have also been demonstrated [42]–[45]. For our purposes, the use of resistive liquid metal sensors was based on a combination of experience and expected device performance. We have extensive knowledge of how to manufacture this class of devices, and during the design phase we anticipated that the performance would be sufficient to achieve our goal of state reconstruction.

In summary, there have been many approaches taken to developing sensory skins. The majority of these concepts have used resistive sensors, as our approach uses. However, many of the sensor skins described in the literature contain inextensible elements, making integration with highly deformable bodies difficult. Our long-term objective is to create highly deformable sensory skins, which has caused us to focus on silicone elastomer substrates. Liquid metal is attractive to us in this application given its potential for high deformations and low stiffness. For these reasons, it can be integrated into a soft sensor skin without negatively impacting the mechanical response of the skin. Finally, we have chosen to develop a novel patterning approach to creating traditional microchannels. While the channels created in this way are rougher than those produced via molding, laser-based ablation is much more scalable and compatible with large-scale manufacturing processes such as roll-to-roll fabrication.

III. Experimental

A. Module Fabrication

The sensory skin modules created for this work were fabricated from two sheets of elastomer sandwiching liquid-metal-filled microchannels. We used two platinum-cure silicone elastomers: Smooth-Sil 950 (Smooth-On) and Sylgard 184 (Dow Corning). Both of these elastomers are received as two liquid parts that are mixed 10:1 by mass. Once the two parts are added to a plastic cup, we pre-mix the elastomer by hand using a plastic knife to ensure proper blending, followed by mixing and degassing in a THINKY ARE-310 orbital mixer. The resulting mixed elastomer is ready to cast. The following steps of the fabrication process are illustrated in Fig. 3.

We prepared the elastomer films, which we call substrates, used in these experiments using a “rod-coating” technique. This approach is borrowed from the coating industry, and is frequently employed to create uniform coatings on long host substrates. Our purpose in using this method instead of the more conventional spin-coating approach is that spin coating is limited to the size of the substrate that can be created. The elastomer substrate limits the host substrate onto which it is cast. The most common host substrate used in the soft robotics

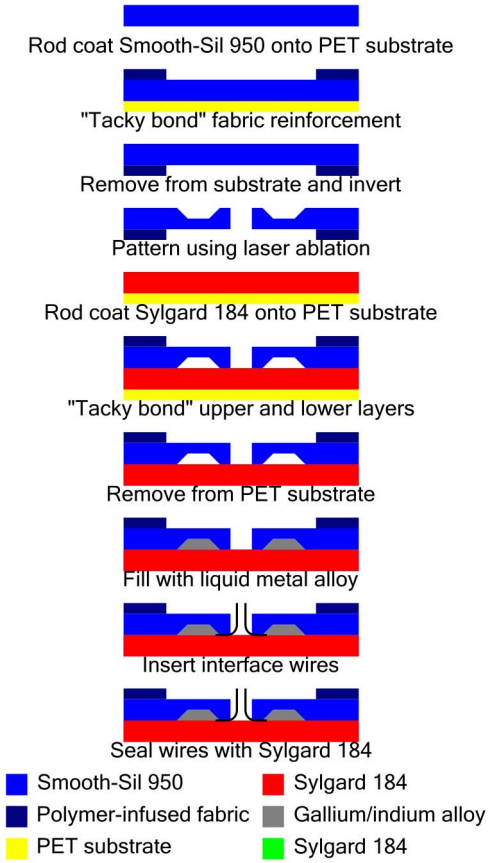

Fig. 3. Fabrication sequence used to manufacture modules.

literature is a silicon wafer. With rod coating, we were able to create substrates on the meter scale, which enabled us to produce many (typically 10-12) sensor modules from a single substrate.

The first step in the rod coating procedure was to place a host substrate onto a flat surface. In our experiments, we used polyethylene terepthalate (PET) on a laboratory counter top. This film was held in place by Scotch tape to keep it flat and mitigate wrinkling. We prepared liquid elastomer using the procedure discussed above. We typically prepared approximately $60g$ of elastomer, which resulted in a substrate $10cm$ wide by $1m$ long. The final dimensions of the substrate are not important to the performance of the device, since the sensor modules are cut out from the substrate in a later step. The coating rod is the placed on the PET film, at one edge of the film. For these experiments, we used $12'' \times 1/2''$-13 Acme threaded rod (McMaster-Carr). Liquid elastomer is then poured onto the PET film in front of the rod. The elastomer substrate is created by scraping the liquid elastomer across the PET film using the threaded rod. The liquid elastomer flows through the threads of the rod, resulting in a pattern of ridges of liquid behind the rod. Since the geometry of the ridges is determined by the geometry of the rod, the ridges are uniform across the length of the substrate, resulting in a uniform final substrate thickness. Over the next few minutes, the liquid elastomer in the ridges spreads out, resulting in a flat, uniform substrate over a large area. Although we have not demonstrated it in this work, we point out that semi-continuous

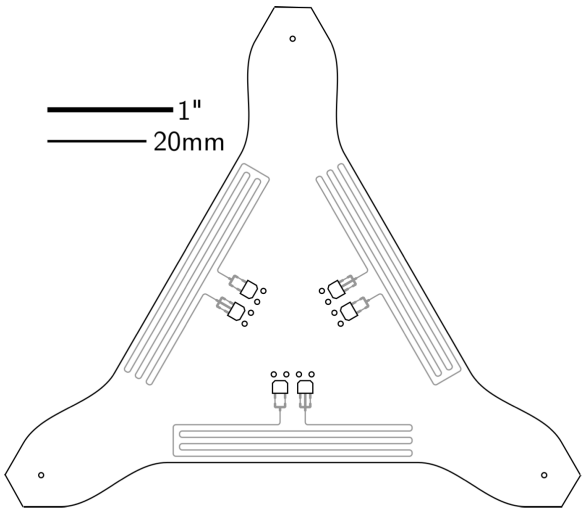

Fig. 4. Schematic drawing of the module. Black lines are cuts in the material, while gray lines are microchannels. The serpentine patterns near the edges of the triangular body are the strain sensitive elements. The rectangular features near the middle of the body are access ports through which the microchannels are filled. The circles near the center of the body are pass-throughs for copper wires from the microchannels on the bottom side of the device to the top of the device. The thicker line in the upper left corner of the image is $1''$, the thinner line is $20mm$.

elastomer substrates could be prepared in this way using roll-to-roll processing equipment.

We measured the resulting substrate thickness with a Zeta 20 optical microscope (Zeta Instruments) with the ability to measure sub-micron variations in thickness and determined that the thickness was $283 \pm 48.4\mu m$. This was based on 10 observations across the prepared substrate. We should note that approximately $1cm$ around the edge of the substrate is visibly thinner, and should not be used. Although the variation is higher than what is observed in spin-coating at similar thicknesses, the variation does not effect sensor performance, and the substantial increase in substrate size makes this method preferable.

We attached fabric reinforcements to the Smooth-Sil 950 base substrate to make the mounting holes in the finished device more robust. We began by manually pressing uncured liquid pre-elastomer into pieces of muslin fabric, then pressed the infused fabric to the upper side of the Smooth-Sil 950 while the latter was partially cured. Bonding to a partially cured substrate was found to have superior mechanical performance than bonding to a fully cured substrate. Partial curing to achieve a tacky state required approximately one hour at room temperature, depending on ambient environmental conditions.

Once the base substrate had cured overnight at room temperature, it was ready for patterning. In order to pattern the substrate, we used a Universal Laser Systems VLS2.30 laser system with a $30W$ CO_2 laser module emitting at a wavelength of $10.6\mu m$. This allowed us to directly pattern the substrate without the use of a mold. The sensor skin pattern is shown in Fig. 4. Once patterned, we cleaned the features by vigorous scrubbing with a paper towel soaked with acetone, followed by sonication in a Branson 1800 bath sonicator, followed by washing the sensor array in acetone, isopropanol, ethanol, and distilled water.

Thorough cleaning is a critical step in our laser-based fabrication process which produces substantial amounts of soot. This step is not required in mold-based processes. However, we believe that the ability to pattern large substrate without having to manufacture a mold makes up for this deficiency. We have found that a combination of mechanical and chemical cleaning is required to adequately clean the surface of the substrates after laser processing. We have selected the combination of acetone, isopropanol, and ethanol by balancing their cleaning abilities with the damage caused to the parts. Toluene, for example, is a superior cleaning agent, but causes $>10\%$ shrinkage of the parts. We have found that a simple visual inspection is sufficient to determine when a part is sufficiently clean. In the case of the Smooth-Sil 950 used in these experiments, the substrate is blue, while the soot resulting from the laser ablation process is white, making it easy to identify on the surface. If any soot is observed after cleaning, the part is re-cleaned using the procedure described above.

To complete the device, we prepared another elastic substrate of Sylgard 184 using the same rod coating method. Depending on ambient humidity, curing the Sylgard 184 for 12 to 18 hours at room temperature resulted in a tacky consistency. We placed the patterned base substrate, channels down, onto the surface of the partially cured substrate, working slowing to minimize the bubbles between the layers. This sandwich is allowed to cure for at least one day to complete the bonding. We have found that tacky bonding has superior adhesion to plasma bonding, and substantially lower probability of filling channels relative to using a liquid "glue" layer. These results are consistent with the findings of Eddings, *et al* [46]. Once bonded, a final patterning step was performed to cut the sensor skin to its final size using the VLS 2.30 laser patterning system. The completed elastomer module is shown in Fig. 1.

At this point, the elastomer module is complete, but does not contain sensor elements. The last step in the assembly process is to fill the microchannels created via laser patterning with eutectic gallium indium alloy. We do this by injecting the liquid metal into the microchannels using a syringe and needle. Once filled, we insert enamel-coated 34Ga copper wires with approximately $1cm$ of insulation stripped from each end into the ports illustrated in Fig. 4. To finalize the module, droplets of Sylgard 184 are used to seal the fill ports and wires.

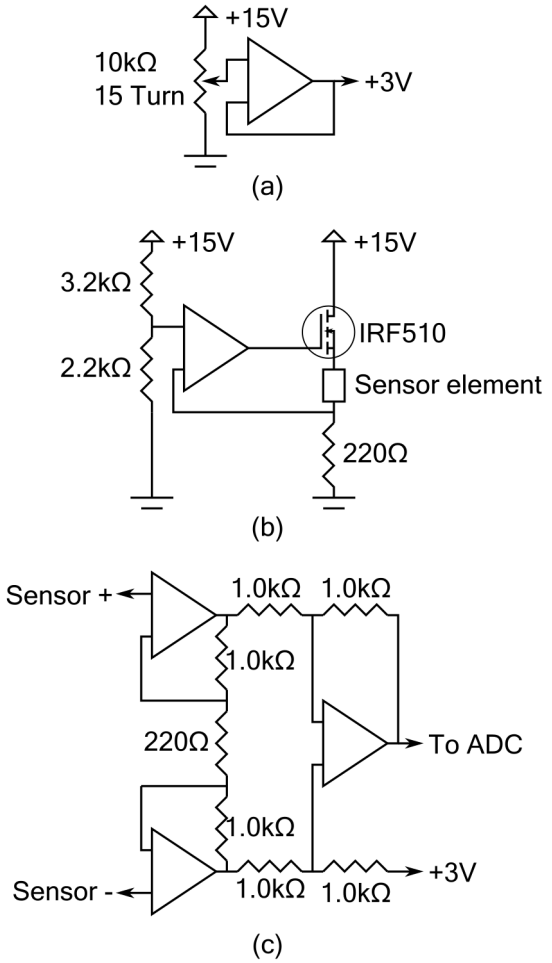

Fig. 5. Electronics used for signal conditioning. Part (a) depicts the voltage reference. The voltage reference was set to 3.00V using the potentiometer. Part (b) depicts the transimpedance amplifier used to provide constant current through the sensor. Part (c) depicts the differential amplifier used to measure the voltage drop across the sensor element and output the result to an ADC on an Arduino microcontroller (not shown). A single instance of the voltage reference was used. Parts (b) and (c) were repeated three times to provide parallel measurements of the three resistive strain elements on a single sensor. The circuits in Parts (b) and (c) were implemented using a single quad op amp for each channel.

B. Measurement of Strain via Changes in Resistance

The resistance of the sensors embedded along the edges of the structure changes as a function of strain. As the resistance of each element is less than 10Ω, compensating for the effects of contact resistance becomes important. Our measurements indicate that contact resistance is approximately 1Ω across both interfaces, and changes in response to changes in wetted (conducting) area due to inconsistent adhesion between the liquid metal and interface electrodes. Therefore, we employed a four-wire approach. We supply a fixed current to the outer two terminals, while measuring the voltage drop across the inner terminals. Signal conditioning was accomplished using a custom-built breadboard composed of three channels read by an Arduino Uno R3 microcontroller connected via USB to a PC running Ubuntu 14.04. Each channel of the signal conditioning breadboard was composed of a transconductance amplifier to supply constant current to the resistive strain gauge element and a differential amplifier to measure the voltage drop across the gauge. These electronics are shown in Fig. 5.

The modules were tested by pinning the three ends at an array of locations. We used a polystyrene sheet (McMaster-Carr) with a laser-cut pattern of holes to conduct this test. 3D printed "push-pins" were used to pin the module to the polystyrene sheet. We tested various configurations such that the strain between nodes varied from 0% to 25%. We note here that we are not interested in the true strain in the strain gauge. We understand that the strain between nodes and the strain in the gauge will be different due to variation in how the module membrane deforms. However, as we are measuring the response of the resistive element and comparing it to the nodal displacement, the actual strain

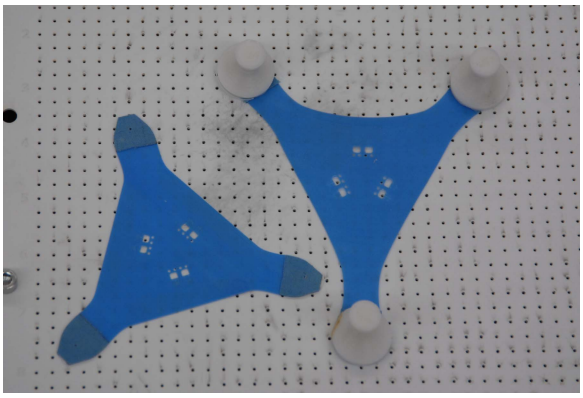

Fig. 6. Unstretched (left) and stretched (right) modules on polystyrene pegboard (background). 3D printed pegs are visible at the ends of the stretched module. Pins protrude from the pegs, through the module, and into the holes in the pegboard. Pins are held in the board by friction. Note that electrical lead wires have been removed from these devices for clarity. The holes in the pegboard are 1/4″ apart.

in the gauge is unimportant. The pegboard used in this experiment, with a module in place, is shown in Fig. 6.

We used a script written in Python to select test configurations at random and to read the strain gauge data through the Arduino Uno R3 microcontroller. During the test, the program would select a combination of holes to pin the module to, wait for the operator to pin the module at the required location, then read and record the data. The experimental matrix consisted of 156 observations of 56 unique configurations. Each observation included measurements of all three strain gauges in each module. The measurements performed in this study are quasi-static. However, our previous work indicates that loading rate is minor effect in elastomer sensors made from these materials, up to $100mm.min^{-1}$ [47]. In our intended robotic application, we do not foresee loading rates which would cause a significantly different response than observed in these quasi-static tests.

The baseline resistance, R_0, was measured once for each strain gauge before the test sequence and once after. The baseline resistance used for the computations described below was the average of those two observations. The baseline resistance of the sensors, across all three modules used in the tests, was $3.75 \pm 0.373\Omega$ (95% confidence, $n = 18$). The sequence of 156 measurements took between 6 to 8 hours to complete. The average change in undeformed resistance between the start and end of the test across all tests was $0.108 \pm 0.504\Omega$ (95% confidence, $n = 9$). Excluding one test which was a clear outlier, this reduces to $0.0354 \pm 0.0387\Omega$ (95% confidence, $n = 8$). This outlier was element 1 on module 3, which is visible in Fig. 7(c). We have included this data in all other calculations. The change in resistance of 0.0354Ω is 0.943% of the undeformed resistance, which we believe is sufficiently low that it can be neglected. Therefore, we are comfortable using only two measurements of baseline resistance. We also note that the stability of the baseline over this extensive series of deformations suggests the utility of this device in real-world applications such as robotic proprioception. For a detailed analysis of the response of this type of liquid-embedded elastomer strain sensor, including studies of loading rate, cyclic load, and stress relaxation, we suggest our recently published work [47].

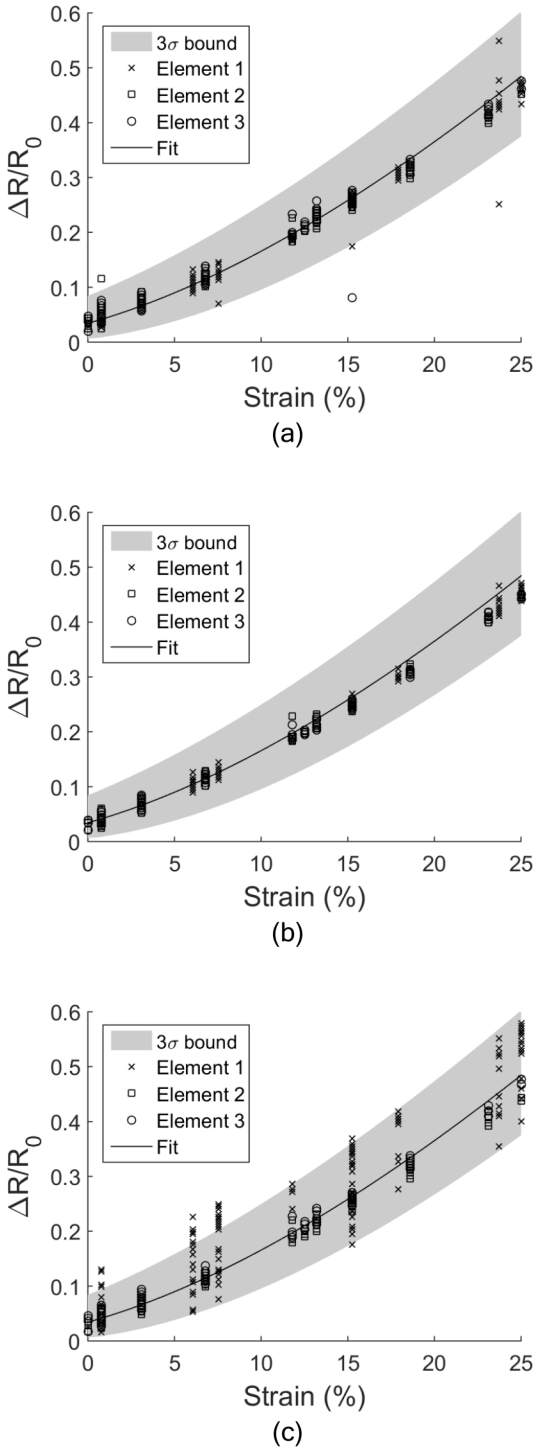

Fig. 7. Normalized change in resistance as a function of strain for three modules. Images (a)-(c) show data for modules 1-3, respectively. Points are experimentally measured resistance values for the three strain gauges on the device. The solid line represents the least squares approximation of the data. The shaded region represents the 3σ confidence interval taken over all of the data. Note that the same calibration was used for all three modules, indicating repeatiblity across modules and between resistive elements within a module.

IV. Results

Fig. 7 shows the response for three modules. The experimental data in these figures were obtained by fixing the geometry using the pegboard discussed previously and measuring the change in resistance. In each figure, the data for all three strain gauges of a given module are presented. The strain in the horizontal axis is only the strain along the side of the corresponding strain gauge. The coupling between the output of a gauge and the strain in the opposite sides of the triangular array are negligible. For example, the data for element 1 is plotted against the strain in side 1, regardless of the strain in sides 2 and 3.

The least squares fit curve in the figures represents the inverse problem, where the normalized change in resistance is treated as the measured value, and strain is the value to be determined. The inverse problem is representative of how the modules will be used in practice. We considered a simplified resistive strain gauge to provide a theoretical basis for our model. We made the assumptions that the conductive liquid metal within the strain gauge is incompressible, and that the cross-section of the conductive trace is constant throughout its length. This latter assumption was confirmed by cross-section measurements of the channels with a Zeta 20 optical microscope (Zeta Instruments). The volume of the liquid metal, which is conserved, is therefore:

$$V = 6L_0A \tag{1}$$

where A is the initial cross-sectional area, L_0 is the undeformed length, and the factor 6 accounts for the 6 parallel paths in the strain sensor (see Fig. 4). The deformed cross-section is:

$$A^* = \frac{6L_0A}{6L^*} = \frac{L_0A}{L^*} = \frac{L_0A}{L_0+\delta} \tag{2}$$

where A^* is the cross-section in the deformed state, L^* is the deformed length, and δ is the magnitude of the deformation. We can relate the deformation to the strain by $\delta = \epsilon L_0$. Substituting and canceling out L_0, we find that:

$$A^* = \frac{A}{1+\epsilon} \tag{3}$$

The resistance is given by:

$$R_0 = \frac{\rho L_0}{A} \tag{4a}$$

$$R^* = \frac{\rho L^*}{A^*} \tag{4b}$$

where R_0 and R^* are the initial and deformed resistances, respectively. The change in resistance is therefore:

$$\Delta R = \frac{\rho L^*}{A^*} - \frac{\rho L_0}{A} \tag{5}$$

The normalized change in resistance is:

$$\frac{\Delta R}{R_0} = \frac{AL^* - A^*L_0}{A^*L_0} \tag{6}$$

Substituting the expressions for A^* and L^* into this equation results in the final form of the normalized change in resistance:

$$\frac{\Delta R}{R_0} = \epsilon(2+\epsilon) \tag{7}$$

This equation is inverted to find a relationship between the normalized change in resistance, which is measured, to the strain:

$$\epsilon = -1 + \sqrt{1 + \frac{1}{4}\frac{\Delta R}{R_0}} \tag{8}$$

In order to fit the data, we used a generalized least squares approach. Given the quadratic relationship between strain and normalized change in resistance from the proceeding analysis, we assumed a model in the form:

$$\epsilon = a_0 + a_1 r + a_2 r^{0.5} \tag{9}$$

where ϵ is the applied strain and r is the normalized change in resistance, namely $r = \frac{\Delta R}{R_0}$.

We created Equation 9 by inspection. The non-linear term came from inspecting the previous equation and noting that $\Delta R/R_0$ appears with a power $1/2$. There are two non-idealities that complicate this expression. The offset term, a_0, is due to prestrain caused by material shrinkage. The strain between nodes is computed based on a nominal initial length. However, during curing, the elastomer contracted slightly, resulting in a initial, unstrained node-node spacing that was smaller than the nominal. The linear term a_1 is due to the difference between the node to node strain and the strain observed in the sensing element. Due to the geometry of the module, the strain observed in the interior of the triangular module where the sensors are located was less than that applied to the exterior, necessitating the use of a scaling factor.

With this, we cast our experimental data in the form:

$$\begin{bmatrix} 1 & r_0 & r_0^{0.5} \\ 1 & r_1 & r_1^{0.5} \\ 1 & r_2 & r_2^{0.5} \\ & \vdots & \end{bmatrix} \begin{bmatrix} a_0 \\ a_1 \\ a_2 \end{bmatrix} = \begin{bmatrix} \epsilon_0 \\ \epsilon_1 \\ \epsilon_2 \\ \vdots \end{bmatrix} \tag{10}$$

where r_i is the normalized change in resistance of the i^{th} measurement, ϵ_i is the applied strain of the i^{th} measurement, and a_i are the parameters of the fit. We express this system as:

$$\mathbf{Ra} = \mathbf{s} \tag{11}$$

The least-squares fit of this experimental data is:

$$\mathbf{a} = (\mathbf{R}^T\mathbf{R})^{-1}\mathbf{R}^T\mathbf{s} \tag{12}$$

Using the data in Fig. 7, we found that the parameters of the fit are:

$$\mathbf{a} = [-0.07320, 0.1342, 0.3711]^T \tag{13}$$

This solution is what was used to draw the solid lines on Fig. 7.

Based on the least squares approximation, we also computed the error between the approximation and the actual data. These errors, across all three elements on three arrays (nine total elements) are presented as a histogram in Fig. 8. Using this data, we found that the standard deviation (σ) in the error in estimated strain is 0.0152, which is 6.08% of the full-scale.

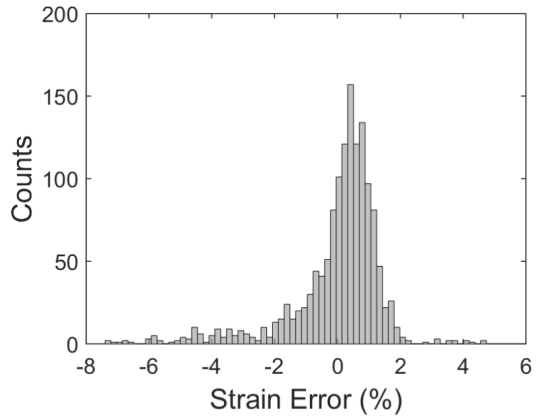

Fig. 8. Histogram showing error between applied and computed strain across all strain gauges and modules. Computed strain is based on the measured normalized change in resistance and the least squares fit of the data. Zero error represents no difference between the reconstructed strain and the applied strain.

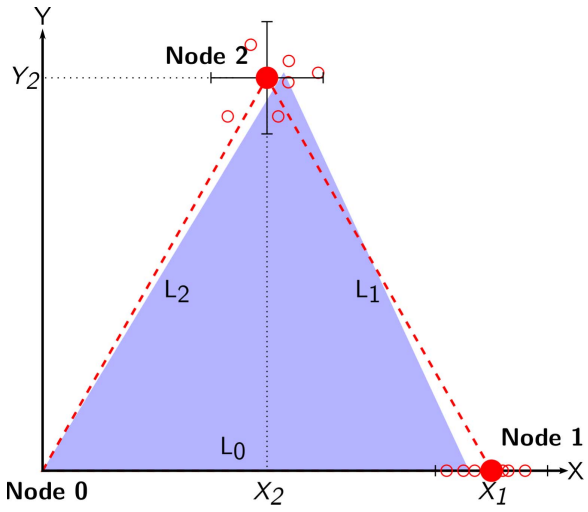

Fig. 9. Example state reconstruction geometry. The solid blue triangle represents the true geometry of the module. The solid red circles represent the reconstruced locations of the nodes based on the measured resistance. The red dashed lines connect the solid red circles. The hollow red circles represent the reconstructed locations of the nodes based on the perturbed length values. Only six such perturbed estimates are shown in the figure, although 100 samples were used in practice. The error bars shown on the nodes are based on the observed standard deviation in the reconstructed node positions (hollow red circles). The geometry in this figure is notional, and errors have been exaggerated for clarity.

Finally, we reconstructed geometry based on measured resistance values. Since the modules have no way to establish their position in a global sense, we applied a local coordinate system. This coordinate system was centered at one node of the module, and the X coordinate passing through another node. We show the labeled geometry in Fig. 9. The nominal coordinates (in inches) of the nodes were $(0.0, 0.0)$, $(4.0, 0.0)$, and $(2.0, 3.5)$. Let L_0 be the distance between nodes 0 and 1, L_1 be the distance between nodes 1 and 2, and L_2 be the distance between nodes 2 and 0. In terms of strain, these

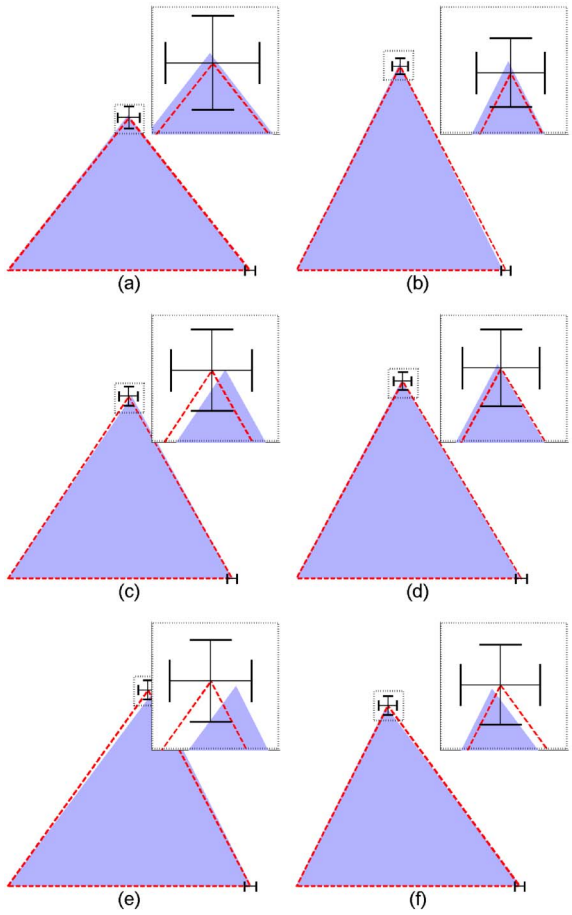

Fig. 10. Reconstructed sensor geometry shows the comparison between the reconstructed geometry based on the resistance measurements (red dashed line) and the known deformed geometry (solid blue triangle) for three measurements (a-c). Error bars around the nodes represent the 3σ uncertainty bounds. There are no error bars around the lower left node as that node is defined as the origin of the coordinate system. The only uncertainty in the position of the node at the lower right is in the horizontal direction, as the vertical position is defined to be zero. The inset shows an enlargement of the area around the upper node. The dimensions of the inset are $15mm \times 15mm$.

lengths were:

$$L_0 = L(1 + \epsilon_0) \tag{14a}$$
$$L_1 = L(1 + \epsilon_1) \tag{14b}$$
$$L_2 = L(1 + \epsilon_2) \tag{14c}$$

where L is the undeformed length of a side. Based on the definition of the local coordinate system, $x_0 = y_0 = y_1 = 0$. The remaining positions were specified by:

$$x_1 = L_0 \tag{15a}$$
$$x_2 = \frac{L_2^2 - L_1^2 + x_1^2}{2x_1} \tag{15b}$$
$$y_2 = \sqrt{L_2^2 - x_2^2} \tag{15c}$$

To compute the strain, ϵ_i, in Equation 14, we used the model presented in Equation 9, with the coefficients from

Equation 13. The resistance values were measured directly from the strain gauges.

We used a perturbation approach to determine the relationship between the uncertainty in the gauge lengths and the node positions. Since the relationship between the error in the measured lengths and the positions of the nodes is non-linear and depends on the configuration of the module, we use a Monte Carlo approach to estimate the uncertainties. To perform this analysis, we assumed that the errors in the gauge measurements were uniformly distributed with $3\sigma = 0.0456$. This matches the distribution observed in Fig. 8 and includes a factor of 3 to include 3σ uncertainties. To begin the analysis, we started with the nominal gauge measurements, then applied a randomly drawn perturbation based on the distribution described above. We then computed the resulting node positions, based on Equations 14(a-c). The resulting positions are shown as open red circles in Fig. 9. We repeated this random draw procedure 100 times to develop a population for statistical analysis (only six such positions are shown in the figure for clarity). We computed the geometric distance between the nominal node location and each perturbed location and developed an error distribution based on this measure. From that distribution, we computed the uncertainty in the reconstructed node position. Reconstructed triangles with uncertainty estimates are shown along with known geometry in Fig. 10. The six figures shown are representative of the full set of experiments.

V. Conclusion

In this paper we have demonstrated the fabrication and performance of a multi-element resistive strain gauge module for state measurement. This device is an important building block for soft sensory skins. We have demonstrated that the manufacturing process is consistent between modules, and that strain gauges across different modules, as well as within each modules, have similar performance characteristics. Further, we demonstrate that even with the current rudimentary signal conditioning approach we have achieved sufficient accuracy to be of use in many soft robotic applications.

One of the significant limitations in the present work is the interconnection between the modules and the signal conditioning electronics. The current electronics implementation hinders the application of these modules to soft robots and limits mobility of the test apparatus. In the future, we will focus on integrating the signal conditioning into the elastomer substrate. We believe this is the next step towards state-aware sensor skins fabricated from elastomeric materials.

Acknowledgment

The authors wish to thank Michelle Yuen for her contributions in the design and manufacturing of the polymer-infused reinforcement tabs on the ends of the sensor arrays.

Any opinion, findings, and conclusions or recommendations expressed in this material are those of the authors and do not necessarily reflect the views of the National Science Foundation or the National Aeronautics and Space Administration.

References

[1] C. Liu, "Recent developments in polymer MEMS," *Adv. Mater.*, vol. 19, no. 22, pp. 3783–3790, Nov. 2007. [Online]. Available: http://onlinelibrary.wiley.com.ezproxy.lib.purdue.edu/doi/10.1002/adma.200701709/abstract

[2] S. Nambiar and J. T. W. Yeow, "Conductive polymer-based sensors for biomedical applications," *Biosensors Bioelectron.*, vol. 26, no. 5, pp. 1825–1832, Jan. 2011. [Online]. Available: http://www.sciencedirect.com/science/article/pii/S095656631000672X

[3] B. O'Brien, T. Gisby, and I. A. Anderson, "Stretch sensors for human body motion," *Proc. SPIE*, vol. 9056, p. 905618-1–905618-9, 2014. [Online]. Available: http://dx.doi.org/10.1117/12.2046143

[4] M. A. Schmidt, R. T. Howe, S. D. Senturia, and J. H. Haritonidis, "Design and calibration of a microfabricated floating-element shear-stress sensor," *IEEE Trans. Electron Devices*, vol. 35, no. 6, pp. 750–757, Jun. 1988.

[5] F. Jiang, Y.-C. Tai, K. Walsh, T. Tsao, G.-B. Lee, and C.-M. Ho, "A flexible MEMS technology and its first application to shear stress sensor skin," in *Proc. IEEE 10th Annu. Int. Workshop Micro Electro Mech. Syst. (MEMS)*, Jan. 1997, pp. 465–470.

[6] Y. Xu, F. Jiang, S. Newbern, A. Huang, C.-M. Ho, and Y.-C. Tai, "Flexible shear-stress sensor skin and its application to unmanned aerial vehicles," *Sens. Actuators A, Phys.*, vol. 105, no. 3, pp. 321–329, Aug. 2003. [Online]. Available: http://www.sciencedirect.com/science/article/pii/S0924424703002309

[7] Y. Xu, J. Clendenen, S. Tung, F. Jiang, and Y.-C. Tai, "Underwater flexible shear-stress sensor skins," in *Proc. 17th IEEE Int. Conf. Micro Electro Mech. Syst. (MEMS)*, 2004, pp. 833–836. [Online]. Available: http://ieeexplore.ieee.org/xpls/abs_all.jsp?arnumber=1290714

[8] J. Engel, J. Chen, C. Liu, B. R. Flachsbart, J. C. Selby, and M. A. Shannon, "Development of polyimide-based flexible tactile sensing skin," in *Symposium D Electronics on Unconventional Substrates–Electrotextiles and Giant-Area Flexible Circuits* (MRS Proceedings), vol. 736, 2002. DOI: 10.1557/PROC736D4.5. [Online]. Available: http://journals.cambridge.org/article_S1946427400145105

[9] J. Engel, J. Chen, and C. Liu, "Development of polyimide flexible tactile sensor skin," *J. Micromech. Microeng.*, vol. 13, no. 3, pp. 359–366, May 2003. [Online]. Available: http://stacks.iop.org/0960-1317/13/i=3/a=302?key=crossref.8087244fda1061abf6dc04e3c3a02588

[10] J. Engel, J. Chen, Z. Fan, and C. Liu, "Polymer micromachined multimodal tactile sensors," *Sens. Actuators A, Phys.*, vol. 117, no. 1, pp. 50–61, Jan. 2005. [Online]. Available: http://www.sciencedirect.com/science/article/pii/S0924424704003875

[11] J.-H. Kim, J.-I. Lee, H.-J. Lee, Y.-K. Park, M.-S. Kim, and D.-I. Kang, "Design of flexible tactile sensor based on three-component force and its fabrication," in *Proc. IEEE Int. Conf. Robot. Autom. (ICRA)*, Apr. 2005, pp. 2578–2581.

[12] E.-S. Hwang, J.-H. Seo, and Y.-J. Kim, "A polymer-based flexible tactile sensor for normal and shear load detection," in *Proc. 19th IEEE Int. Conf. Micro Electro Mech. Syst. (MEMS)*, Istanbul, Turkey, Jan. 2006, pp. 714–717.

[13] E.-S. Hwang, J.-H. Seo, and Y.-J. Kim, "A polymer-based flexible tactile sensor for both normal and shear load detections and its application for robotics," *J. Microelectromech. Syst.*, vol. 16, no. 3, pp. 556–563, Jun. 2007.

[14] A. Firouzeh and J. Paik, "The design and modeling of a novel resistive stretch sensor with tunable sensitivity," *IEEE Sensors J.*, vol. 15, no. 11, pp. 6390–6398, Nov. 2015.

[15] Y. J. Yang *et al.*, "An integrated flexible temperature and tactile sensing array using PI-copper films," *Sens. Actuators A, Phys.*, vol. 143, no. 1, pp. 143–153, May 2008. [Online]. Available: http://www.sciencedirect.com/science/article/pii/S0924424707008126

[16] T. V. Papakostas, J. Lima, and M. Lowe, "A large area force sensor for smart skin applications," in *Proc. IEEE Sensors*, vol. 2, Jun. 2002, pp. 1620–1624. [Online]. Available: http://ieeexplore.ieee.org/xpls/abs_all.jsp?arnumber=1037366

[17] V. Duchaine, N. Lauzier, M. Baril, M.-A. Lacasse, and C. Gosselin, "A flexible robot skin for safe physical human robot interaction," in *Proc. IEEE Int. Conf. Robot Autom (ICRA)*, May 2009, pp. 3676–3681.

[18] K. Takei *et al.*, "Nanowire active-matrix circuitry for low-voltage macroscale artificial skin," *Natural Mater.*, vol. 9, no. 10, pp. 821–826, Oct. 2010. [Online]. Available: http://www.nature.com/nmat/journal/v9/n10/abs/nmat2835.html

[19] J. A. Dobrzynska and M. A. M. Gijs, "Flexible polyimide-based force sensor," *Sens. Actuators A, Phys.*, vol. 173, no. 1, pp. 127–135, Jan. 2012. [Online]. Available: http://www.sciencedirect.com/science/article/pii/S0924424711006637

[20] M. Kujawski, J. D. Pearse, and E. Smela, "Elastomers filled with exfoliated graphite as compliant electrodes," *Carbon*, vol. 48, no. 9, pp. 2409–2417, Aug. 2010. [Online]. Available: http://www.sciencedirect.com/science/article/pii/S000862231000151X

[21] M. G. King, A. J. Baragwanath, M. C. Rosamond, D. Wood, and A. J. Gallant, "Porous PDMS force sensitive resistors," *Procedia Chem.*, vol. 1, no. 1, pp. 568–571, Sep. 2009. [Online]. Available: http://www.sciencedirect.com/science/article/pii/S1876619609001430

[22] T. Yamada *et al.*, "A stretchable carbon nanotube strain sensor for human-motion detection," *Nature Nanotechnol.*, vol. 6, no. 5, pp. 296–301, May 2011. [Online]. Available: http://www.nature.com/nnano/journal/v6/n5/full/nnano.2011.36.html

[23] L. Cai *et al.*, "Super-stretchable, transparent carbon nanotube-based capacitive strain sensors for human motion detection," *Sci. Rep.*, vol. 3, Oct. 2013, Art. ID 3048. [Online]. Available: http://www.nature.com/doifinder/10.1038/srep03048

[24] M. Amjadi, Y. J. Yoon, and I. Park, "Ultra-stretchable and skin-mountable strain sensors using carbon nanotubes–Ecoflex nanocomposites," *Nanotechnology*, vol. 26, no. 37, p. 375501, Sep. 2015. [Online]. Available: http://stacks.iop.org/0957-4484/26/i=37/a=375501?key=crossref.b6de8dc9e8a87a924c7c1283b1dabba6

[25] D. Zhou and H. Wang, "Design and evaluation of a skin-like sensor with high stretchability for contact pressure measurement," *Sens. Actuators A, Phys.*, vol. 204, pp. 114–121, Dec. 2013. [Online]. Available: http://www.sciencedirect.com/science/article/pii/S0924424713004858

[26] C. Yan *et al.*, "Highly stretchable piezoresistive graphene–nanocellulose nanopaper for strain sensors," *Adv. Mater.*, vol. 26, no. 13, pp. 2022–2027, Apr. 2014. [Online]. Available: http://onlinelibrary.wiley.com/doi/10.1002/adma.201304742/abstract

[27] M. D. Dickey, R. C. Chiechi, R. J. Larsen, E. A. Weiss, D. A. Weitz, and G. M. Whitesides, "Eutectic gallium-indium (EGaIn): A liquid metal alloy for the formation of stable structures in microchannels at room temperature," *Adv. Funct. Mater.*, vol. 18, no. 7, pp. 1097–1104, 2008. [Online]. Available: http://onlinelibrary.wiley.com/doi/10.1002/adfm.200701216/abstract

[28] Y.-L. Park, C. Majidi, R. Kramer, P. Bérard, and R. J. Wood, "Hyperelastic pressure sensing with a liquid-embedded elastomer," *J. Micromech. Microeng.*, vol. 20, no. 12, p. 125029, Dec. 2010. [Online]. Available: http://iopscience.iop.org/0960-1317/20/12/125029

[29] R. K. Kramer, C. Majidi, and R. J. Wood, "Wearable tactile keypad with stretchable artificial skin," in *Proc. IEEE Int. Conf. Robot. Autom. (ICRA)*, May 2011, pp. 1103–1107.

[30] Y.-L. Park, B.-R. Chen, and R. J. Wood, "Soft artificial skin with multimodal sensing capability using embedded liquid conductors," in *Proc. IEEE Sensors*, Oct. 2011, pp. 81–84.

[31] Y.-L. Park, B.-R. Chen, and R. J. Wood, "Design and fabrication of soft artificial skin using embedded microchannels and liquid conductors," *IEEE Sensors J.*, vol. 12, no. 8, pp. 2711–2718, Aug. 2012.

[32] C. Majidi, R. Kramer, and R. J. Wood, "A non-differential elastomer curvature sensor for softer-than-skin electronics," *Smart Mater. Struct.*, vol. 20, no. 10, p. 105017, Oct. 2011. [Online]. Available: http://iopscience.iop.org/0964-1726/20/10/105017

[33] R. K. Kramer, C. Majidi, R. Sahai, and R. J. Wood, "Soft curvature sensors for joint angle proprioception," in *Proc. IEEE/RSJ Int. Conf. Intell. Robots Syst. (IROS)*, Sep. 2011, pp. 1919–1926.

[34] J. K. Paik, R. K. Kramer, and R. J. Wood, "Stretchable circuits and sensors for robotic origami," in *Proc. IEEE/RSJ Int. Conf. Intell. Robots Syst. (IROS)*, Sep. 2011, pp. 414–420.

[35] J. W. Boley, E. L. White, G. T.-C. Chiu, and R. K. Kramer, "Direct writing of gallium-indium alloy for stretchable electronics," *Adv. Funct. Mater.*, vol. 24, no. 23, pp. 3501–3507, Feb. 2014. [Online]. Available: http://doi.wiley.com/10.1002/adfm.201303220

[36] J. W. Boley, E. L. White, and R. K. Kramer, "Mechanically sintered gallium–indium nanoparticles," *Adv. Mater.*, vol. 24, no. 14, pp. 2355–2360, Feb. 2015. [Online]. Available: http://onlinelibrary.wiley.com/doi/10.1002/adma.201404790/abstract

[37] J.-B. Chossat, Y.-L. Park, R. J. Wood, and V. Duchaine, "A soft strain sensor based on ionic and metal liquids," *IEEE Sensors J.*, vol. 13, no. 9, pp. 3405–3414, Sep. 2013.

[38] J.-B. Chossat, Y. Tao, V. Duchaine, and Y.-L. Park, "Wearable soft artificial skin for hand motion detection with embedded microfluidic strain sensing," in *Proc. IEEE Int. Conf. Robot. Autom. (ICRA)*, May 2015, pp. 2568–2573.

[39] H.-K. Lee, S.-I. Chang, and E. Yoon, "A flexible polymer tactile sensor: Fabrication and modular expandability for large area deployment," *J. Microelectromech. Syst.*, vol. 15, no. 6, pp. 1681–1686, Dec. 2006.

[40] H.-K. Lee, S.-I. Chang, and E. Yoon, "Dual-mode capacitive proximity sensor for robot application: Implementation of tactile and proximity sensing capability on a single polymer platform using shared electrodes," *IEEE Sensors J.*, vol. 9, no. 12, pp. 1748–1755, Dec. 2009.

[41] D. P. J. Cotton, I. M. Graz, and S. P. Lacour, "A multifunctional capacitive sensor for stretchable electronic skins," *IEEE Sensors J.*, vol. 9, no. 12, pp. 2008–2009, Dec. 2009.

[42] Y. Ohmura, Y. Kuniyoshi, and A. Nagakubo, "Conformable and scalable tactile sensor skin for curved surfaces," in *Proc. IEEE Int. Conf. Robot. Autom. (ICRA)*, May 2006, pp. 1348–1353.

[43] G. Cannata, M. Maggiali, G. Metta, and G. Sandini, "An embedded artificial skin for humanoid robots," in *Proc. IEEE Int. Conf. Multisensor Fusion Integr. Intell. Syst.*, Aug. 2008, pp. 434–438.

[44] A. Cirillo, P. Cirillo, G. De Maria, C. Natale, and S. Pirozzi, "An artificial skin based on optoelectronic technology," *Sens. Actuators A, Phys.*, vol. 212, pp. 110–122, Jun. 2014. [Online]. Available: http://www.sciencedirect.com/science/article/pii/S0924424714001551

[45] E. Baglini, S. Youssefi, F. Mastrogiovanni, and G. Cannata, "A real-time distributed architecture for large-scale tactile sensing," in *Proc. IEEE/RSJ Int. Conf. Intell. Robots Syst. (IROS)*, Sep. 2014, pp. 1663–1669. [Online]. Available: http://ieeexplore.ieee.org/xpls/abs_all.jsp?arnumber=6942778

[46] M. A. Eddings, M. A. Johnson, and B. K. Gale, "Determining the optimal PDMS–PDMS bonding technique for microfluidic devices," *J. Micromech. Microeng.*, vol. 18, no. 6, p. 067001, Jun. 2008. [Online]. Available: http://stacks.iop.org/0960-1317/18/i=6/a=067001?key=crossref.6da1ef5c3b2a789568d7cffa6ecf307c

[47] J. C. Case, E. L. White, and R. K. Kramer, "Soft material characterization for robotic applications," *Soft Robot.*, vol. 2, no. 2, pp. 80–87, Jun. 2015. [Online]. Available: http://online.liebertpub.com/doi/full/10.1089/soro.2015.0002

Edward L. White received the M.S. degree in mechanical engineering and the M.B.A. degree from the University of Arizona, Tucson, AZ, USA. He is currently pursuing the Ph.D. degree with the Fabrication Laboratory, School of Mechanical Engineering, Purdue University, West Lafayette, IN, USA. His research is focused on making soft-robotic systems more manufacturerable and robust.

Jennifer C. Case received the B.S. degree in mechanical engineering from Northern Illinois University, DeKalb, IL, USA, in 2013. She is currently pursuing the Ph.D. degree in mechanical engineering from Purdue University, West Lafayette, IN, USA. Her research is focused on adding closed-loop control systems to highly deformable robots.

Rebecca K. Kramer received the B.S. degree from Johns Hopkins University in 2007, the M.S. degree from the University of California, Berkeley, in 2008, and the Ph.D. degree from Harvard University in 2012. She is currently an Assistant Professor of Mechanical Engineering with Purdue University. At Purdue, she founded the Fabrication Laboratory, which contains a leading facility for the rapid design, fabrication, and analysis of materially soft and multifunctional robots. Her research interests involve stretchable electronics, soft actuators, soft material manufacturing, and soft-bodied control. She is the recipient of a 2014 NASA Early Career Faculty Award and a 2015 NSF CAREER Award. She was named to the 2015 Forbes' 30 under 30 lists.